Comparison of small-strain stiffness of laboratory synthesized hydrate-bearing sands for different formation methods

Mandeep R. Pandey, Jeffrey A. Priest & Jocelyn L. Hayley
Department of Civil Engineering, University of Calgary, Alberta, Canada

ABSTRACT
Understanding the strength and stiffness of hydrate-bearing sands (HBS) is critical in the economic and safe recovery of methane gas from these hydrate deposits. Results to date from laboratory studies highlight significant scatter in the measured strength and stiffness, which may be due to different hydrate formation methods that are adopted, different sands, effective stress conditions and hydrate saturation. In this paper we summarize the results of small-strain laboratory tests that were carried out on HBS with two different particle size distributions, and utilizing two different hydrate formation methods. Specimens were tested in a specially designed triaxial apparatus with a resonant column drive head which allows both small- and large-strain responses of the specimen to be evaluated. Test conditions, such as temperature, gas consumption, resonance frequency were recorded to fully understand stiffness evolution during hydrate formation. Four HBS specimens were tested with the results showing that the formation method adopted in laboratory affects the stiffness evolution during hydrate formation. The results from this study will help improve our understanding of formation of gas hydrate bearing reservoirs in nature to allow safe methane gas production to meet our long-term energy needs.

RÉSUMÉ
La compréhension de la résistance et de la rigidité des sables porteurs d'hydrates (HBS) est essentielle pour la récupération économique et sûre du méthane de ces dépôts d'hydrates. Les résultats obtenus à ce jour à partir d'études en laboratoire mettent en évidence une dispersion importante de la résistance et de la rigidité mesurées, qui peut être due aux différentes méthodes de formation d'hydrates adoptées, aux différents sables, aux conditions de contrainte effective et à la saturation en hydrates. Dans cet article, nous résumons les résultats d'essais en laboratoire de petites déformations qui ont été effectués sur des HBS avec deux distributions granulométriques différentes et en utilisant deux méthodes de formation d'hydrates différentes. Les spécimens ont été testés dans un appareil triaxial spécialement conçu avec une tête d'entraînement à colonne résonnante qui permet d'évaluer les réponses aux petites et grandes déformations du spécimen. Les conditions d'essai, telles que la température, la consommation de gaz et la fréquence de résonance, ont été enregistrées pour bien comprendre l'évolution de la rigidité pendant la formation d'hydrates. Quatre spécimens HBS ont été testés et les résultats montrent que la méthode de formation adoptée en laboratoire affecte l'évolution de la rigidité pendant la formation des hydrates. Les résultats de cette étude contribueront à améliorer notre compréhension de la formation des réservoirs contenant des hydrates de gaz dans la nature afin de permettre une production sûre de méthane pour répondre à nos besoins énergétiques à long terme.

1 INTRODUCTION

Methane gas hydrate is an ice-like crystalline compound, where methane gas molecules are encaged in a lattice of water molecules. Hydrates form under high pressure and low temperature conditions within sediments on continental margins, and under the permafrost, when sufficient methane gas is freely available (Milkov, 2004; Boswell, 2009; Boswell and Collett, 2011). Methane hydrates are of interest as a possible energy resource owing to the enormous volumes of methane gas that is sequestered in the hydrate within these sediments (Wallmann et al., 2012). The high saturation of methane hydrate observed in coarse-grained sediments, where up to 90% of the pore space can be filled with hydrate (Torres et al., 2008; Lei et al., 2022), and the high intrinsic permeability of the sands, make these sediments a target for energy resource development (Boswell, 2009; Moridis et al., 2011; Boswell and Collett, 2011; Boswell et at., 2016). Despite numerous studies on hydrate systems (Boswell et al., 2012; Wallmann et al., 2012; Kida et al., 2015; Dixit et al., 2019; Moore et al., 2022), the actual process controlling the formation of high saturation hydrate-bearing sands (HBS) is yet to be fully understood.

Some small-scale field tests on permafrost deposits (Dallimore and Collett, 2005; Dallimore et al., 2012,) and marine sediments (Kumar et al., 2014; Yamamoto et al., 2014; Yang et al. 2017, Flemings et al., 2020) have indicated the potential viability of methane production from hydrate deposits. However, the short-term nature of these tests, exacerbated by unforeseen circumstances that have prematurely ended tests (Yamamoto et al., 2014) has prevented the long-term production potential of hydrate deposits being explored. Although numerical simulations have explored the long-term potential (Kurihara et al., 2005; Moridis et al., 2005; Moridis et al., 2010, Myshakin et al., 2019; Ouchi et al., 2022), these simulations require accurate input parameters to give realistic predictions.

As testing of intact natural HBS samples is challenging, laboratory synthesized hydrate-bearing soils have been typically used to develop our foundational understanding of HBS. Studies on laboratory synthesized HBS have investigated behaviors such as stiffness, stiffness evolution, strength, deformation during dissociation, that would be important considerations for long-term

development of hydrates. However, there are notable differences in the behaviors of limited number of natural HBS tested vs laboratory synthesized HBS (Priest and Hayley, 2019). Laboratory tests have typically been performed on fine sands with a narrow particle size distribution (PSD) (Masui et al., 2005; Yun et al., 2007; Kneafsey et al., 2007; Hyodo et al., 2013). However, recent natural core samples, obtained during 2018 Indian National Gas Hydrate Project (NGHP-02) expedition, showed that natural HBS appear to have a much wider PSD and results from limited testing suggested that a wider PSD affected the geomechanical properties of HBS (Priest et al., 2018). To investigate this effect, Pandey et al. (2021) presented some preliminary findings on the geomechanical response of two HBS that had different grain size distributions but with the same hydrate saturations. Significant variations in peak strength and stiffness were observed, which suggested that the distribution of hydrate, and how it interacts with sand grains, was an important component of the observed behavior that might arise during hydrate formation and is governed by the PSD.

To investigate further the potential role of PSD on the geomechanical response of a HBS, and the role different hydrate formation methods may have, this paper presents the results from a series of tests conducted on HBS specimens with different PSDs and different methods of hydrate formation. This paper focuses on resonant column tests to investigate the evolution of small-strain stiffness during hydrate formation. The results were analyzed to gain insight into the impact of hydrate formation methodologies on the small-strain stiffness response for two different sand mixtures.

2 MATERIALS AND METHODS

2.1 Experimental Setup

An Environmental Triaxial Automated System (ETAS) manufactured by GDS Instruments was used for the laboratory testing of HBS. A schematic of the test apparatus and various components are presented in Figure 1. The ETAS consists of Hardin-type resonant column (RC) drive head for small-strain testing and a triaxial loading system for large strain tests. More details on the testing apparatus are provided in Pandey et al. (2021). A 32 MPa advanced pressure-volume controller (PVC) was used to control the back pressure (through the base pedestal) and record the volume of methane gas consumed during hydrate formation.

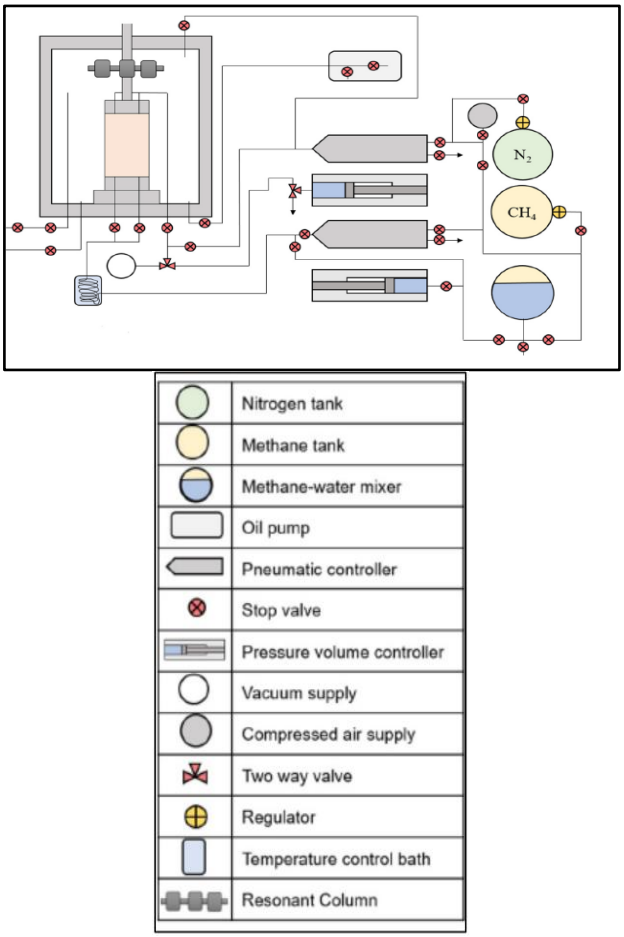

Figure 1. Schematic of ETAS and its components for the testing of hydrate-bearing specimens (from Abbas 2018)

2.2 Soil selection and specimen preparation

Two sands with different PSDs were considered in the testing, namely a coarse sand (CS) and a fine sand (FS). The homogenous distribution of water throughout the length of the sand specimen prior to hydrate formation is an important factor for trying to ensure a uniform hydrate distribution (Minagawa et al., 2009; Howard et al., 2011). Therefore, a series of water retention tests were carried out to determine a PSD that would give a homogenous water distribution within a sand specimen for the target water saturation. Figure 2 highlights the PSDs for the two sands developed, while Figure 3(a) shows the measured water content (w/c) along the length of a coarse sand specimen prior to testing. The sand specimen was formed by tamping an unsaturated sand (at a target water content used in the HBS specimens) and subsequently split into 5 equal layers down the length of the specimen. It can be seen for this coarse sand that only minor difference in w/c are shown along the length of specimen. Figure 3(b) shows the measured water distribution within a HBS specimen after the hydrate formation and subsequent dissociation, showing similar consistency in w/c highlighting the consistency in w/c through the specimen even after testing. Table 1 highlights the properties of each sand mix,

including the D_{10}, D_{50} and D_{90} particle sizes, as well as the minimum and maximum void ratios (e_{max} and e_{min}).

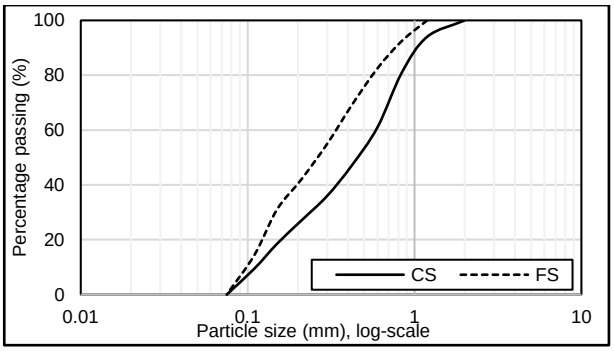

Figure 2. Particle size distributions for the coarse sand (CS) and fine sand (FS) used in this study.

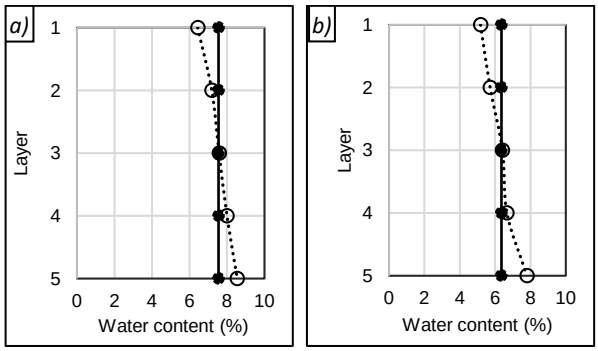

Figure 3. Water distribution on the compacted specimen for CS: *a*) Just after compaction, and *b*) after complete test on hydrate-bearing sand. The open symbols indicate the water content at each layer while the closed symbols show the average water content through the specimen.

Table 1. Basic soil properties

Properties	CS (Coarse)	FS (Fine)
Maximum void ratio (e_{max})	0.82	0.87
Minimum void ratio (e_{min})	0.44	0.49
Mean particle diameter (D_{50})	0.45 mm	0.25 mm
D_{10}	0.12 mm	0.10 mm
D_{90}	1.00 mm	0.80 mm

Sand specimens for testing were formed by hand tamping partially saturated sand in 10 equal layers within a Neoprene membrane within sample mold. The compacted specimens (50 mm diameter and 100 mm height) were transferred to the pressure cell and fixed to the cell base before a suction was applied to the pore space and the mold removed. Local linear variable displacement transducers (LVDT's) were attached over the middle third of the specimen (Figure 4), which included two axial and one radial LVDT's for measuring displacements of specimen during testing. One temperature sensor, located internally at the base of the specimen provided accurate measurement of temperature inside the specimen, while one attached to the membrane on the outside of the specimen is used to measure and control cell temperature.

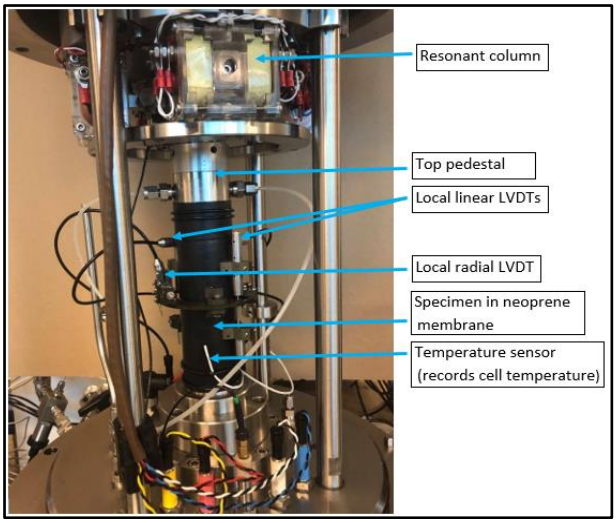

Figure 4. Test specimen in the ETAS setup (from Pandey et al., 2021)

2.3 Hydrate formation methods

In this study hydrates were formed using the excess gas method (Priest et al., 2009), however two different pressure – temperature (P-T) paths were followed for initiating hydrate formation, as highlighted in Figure 5. One P-T path is defined as 'pressure driven' where the gas pressure is increased to reach the hydrate stability region and initiate hydrate formation under constant temperature. This is similar to natural environments where methane gas is generated either in-situ or migrates along permeable pathways, increasing the local pore pressure for a given temperature. The second P-T path is termed 'temperature driven' where the methane gas-charged specimens' temperature is lowered into the hydrate stability region to initiate hydrate formation. This could be similar to the conditions experienced in permafrost regions where propagation of cooler temperatures brought sediments into the hydrate stability region (Collett et al., 2011).

In the pressure-driven formation method that was adopted, methane gas was initially injected at a rate of 100 kPa/min into the partially saturated sand specimen until the pore pressure reached 2500 kPa while maintaining an effective stress of 500 kPa (path 1 in Figure 5). The temperature of specimen was then reduced to 2°C (path 2), which was just outside the hydrate stability zone for the applied pore pressure. After the specimen temperature had stabilized, the methane pore pressure was increased at a rate of 100 kPa/min (path 3) into the hydrate stability region with subsequent initiation of hydrate formation. In this study, all the specimens were tested at a pore pressure of 6000 kPa and a temperature of 2°C (point ***A*** in Figure 5) with an effective stress of 500 kPa. In the temperature driven formation method, methane gas was initially injected into the pore space of the sand up to 6000 kPa while increasing cell pressure to achieve the target effective stress of 500 kPa (path 4). The temperature of the specimen was then reduced (path 5) to bring the specimen into the hydrate stability region and initiate hydrate formation. For this method, the temperature reduction was

carried out in stages to allow RC testing throughout the hydrate formation process to ensure the initial hydrate formation and resulting stiffness evolution was captured.

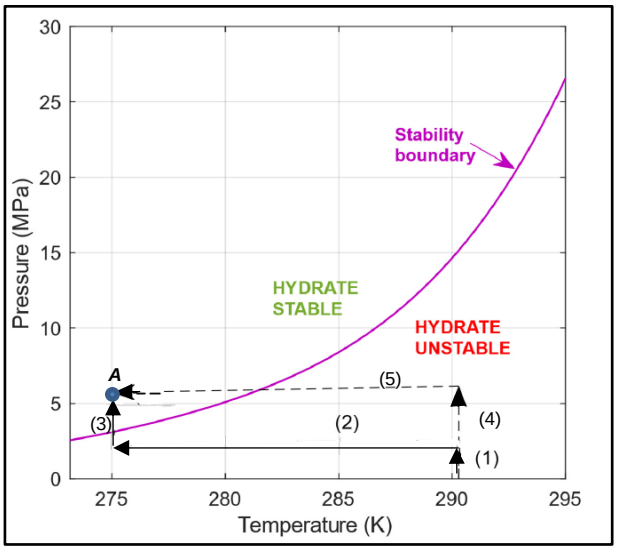

Figure 5. Hydrate phase boundary and the P-T path followed for hydrate formation (Solid lines – Pressure driven; dashed lines – Temperature driven)

Hydrate saturation was calculated using equation [1] assuming all the water was converted to hydrate at a molar ratio of methane to water of 1:5.75 (Sloan and Koh, 2007) at the end of formation process.

$$S_h = \frac{m_w \times M_{hy}}{5.75 \times M_w \times \rho_{hy} \times n \times V_T} \quad [1]$$

Here, m_w is the mass of water added, M_{hy} is the molar mass of methane hydrate (119.63 g/mol), M_w is the molar mass of water (18.015 g/mol), ρ_{hy} is the mass density of methane hydrate (917 kg/m^3), n is the porosity of the specimen and V_T is the total volume of the specimen.

2.4 Test methods

2.4.1 Resonant column (RC) tests

RC tests are non-destructive tests for determining the small-strain stiffness of a specimen. RC tests were performed during hydrate formation to track the stiffness evolution of the HBS and associated specimen damping, and after hydrate formation at increasing strain to determine the modulus reduction properties. The RC apparatus in the ETAS test setup consists of a magnetic drive head connected to the top cap (active end) which in turn is connected to the top of the specimen (Figure 4). A sinusoidal voltage applied to the drive head induces a torsional sinusoidal motion to the top of the specimen, whose frequency can be controlled over a range of frequencies. An accelerometer, mounted on the drive system, is used to measure the resultant motion at the top of the specimen, with the resonant frequency obtained when the sinusoidal motion is in-phase with the applied torque.

Shear modulus (G) was calculated from the resonant frequency and specimen dimensions as outlined in ASTM D-4015-15$^{\varepsilon 1}$ and discussed by Drnevich (1978). At low cyclic strains, shear modulus is considered to be within its elastic range and named G_{max}. At Increasing applied cyclic strain, the threshold for elastic strain is exceeded and a reduction in G is observed. Carrying out RC tests with increasing strain at the end of the hydrate formation stage allows the full strain dependent stiffness of the specimens to be determined that can be utilised in numerical models.

3 RESULTS AND DISCUSSIONS

The details of all the tests including their nomenclature and test conditions are given in Table 2. All the tests were conducted at an effective stress of 500 kPa.

Table 2. Specimen nomenclature, test conditions and measured parameters for all the specimens tested

Specimen*	Porosity (%)	Hydrate Formation method	Hydrate saturation (%)
CS	33.8	*NA*	0
HCS1	36.3	Temperature driven	40.97
HCS2	34.3	Pressure driven	41.85
FS	36.3	*NA*	0
HFS1	40.2	Temperature driven	37.02
HFS2	39.4	Pressure driven	36.49

*CS: Coarse sand, HCS: Hydrate-bearing coarse sand; FS: Fine sand; HFS: Hydrate-bearing fine sand

3.1 Hydrate formation

Figure 6 shows the typical response for forming hydrate using the 'temperature driven' approach. The plot shows the volume of methane gas injected into the specimen (given by the PVC reading) during the reduction in temperature and subsequent hydrate formation. At first the system temperature is reduced to ~8-9ºC (just outside hydrate stability condition) overnight, which leads to a minor increase in methane gas injected into the specimen to compensate for the reduction in pore pressure with temperature. The following morning (~12 hours from start of the test) the temperature was further reduced to 2ºC. After a short period of time in the hydrate stability region, the rapid increase in methane consumption rate, closely followed by a sudden spike in temperature noted by the thermistor (~14.5 hours) in Figure 6 indicates the initiation of exothermic hydrate formation. Considering Figure 6, 90% of the total volume of methane gas was consumed during the first three hours once hydrate started to form. Although not shown here, a similar response in the temperature and rate of initial gas consumption was observed during hydrate formation using the pressure

driven formation method where the specimen temperature was reduced to 2ºC overnight and pressure ramping was carried-out the next morning to reach the target pressure.

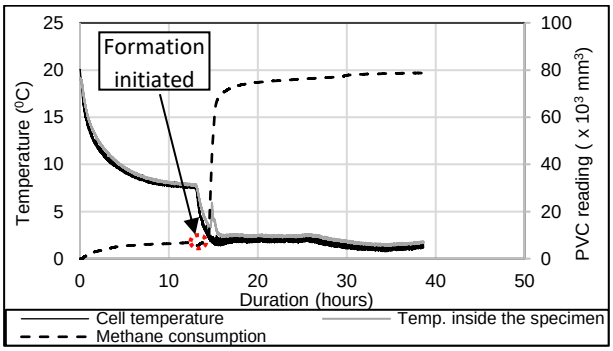

Figure 6. Methane gas consumption due to reduction in temperature and subsequent hydrate formation for Specimen HFS1). The rapid increase in methane consumption resulting from hydrate formation leads to a temperature spike inside the specimen due to exothermic nature of hydrate formation.

3.2 Resonant column tests

Figure 7 highlights the increase in G_{max} (i.e., stiffness evolution) during hydrate formation as evidenced by the rapid increase in methane gas. It can be seen that a rapid increase in G_{max} coincides with the increase in methane gas consumption over the first ~2 hours (hydrate formation). This rapid increase in stiffness is assumed to result from the cementation of sand grains by hydrate because of hydrate forming at grain contacts (Priest et al., 2005; 2009; Sultaniya et al., 2017). Although the majority of hydrate is formed after first three hours (given reduction in gas consumption rate) the specimen stiffness continues to increase suggesting 'Ostwald ripening' of the hydrate grains in the specimen.

Figure 8 shows a comparison between the stiffness evolution and the damping ratio with time during the hydrate formation stage. The damping ratio initially increases with the increase in stiffness, but then reduces to a value similar as that before formation commences. This increase in damping is assumed to result from increasing viscous squirt flow of free water as hydrate forms (Priest et al., 2006). As the hydrate saturation increases, free water in the specimen reduces leading to the reduced squirt flow and therefore less damping. This unique characteristic where high damping is associated with high modulus needs to be studied in detail as this distinct increase in damping ratio with the increase in stiffness of HBS can probably be used to interpret and identify hydrate occurrence in nature (Priest et al., 2006; Liu et al., 2021).

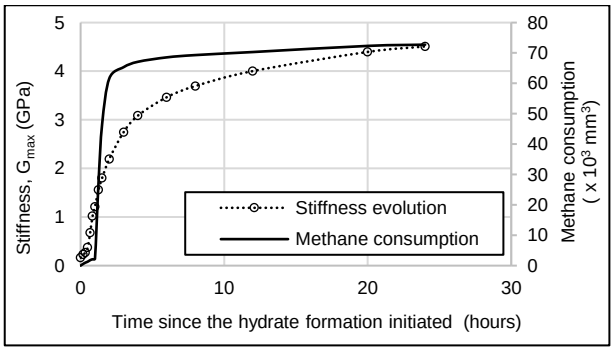

Figure 7. Methane consumption and stiffness evolution during hydrate formation stage (Specimen HFS1) where the specimen stiffness is steadily increasing despite no consumption of methane after ~ 10 hours.

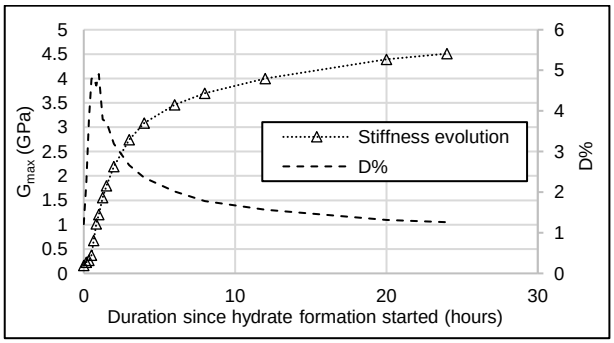

Figure 8. Relationship between stiffness evolution and damping ratio with time during hydrate formation for HFS1.

The stiffness evolution with time for both CS and FS are shown in Figure 9, with time axis shown in minutes commencing at the initiation of hydrate formation. It can be seen that all specimens experience a rapid increase in G_{max}. CS specimens see a more rapid increase in stiffness at the start of hydrate formation than the FS specimens, with the rate of increase reducing significantly around ~500 minutes. This difference in G_{max} evolution may result from differences in water distribution within the sand. The smaller pores of the FS sand may lead to a more patchy water distribution (due to greater suctions) where patches of sands are fully water saturated within the specimen, while the larger pores of the CS may lead to water being at grain contacts. The stiffness of the FS specimens continues to increase slowly up to the maximum measured G_{max} suggesting Ostwald-ripening of the hydrates (Spangenberg et al., 2015) compared to the CS specimens where the stiffness increases rapidly (~500 min), and the rate of increase reduces significantly thereafter. As such, the hydrates in FS may be more influenced by Ostwald-ripening and crystal growth, causing hydrates to exist in patches where hydrate-bearing patches coexist with the completely hydrate-free regions (Dai et al., 2012). Further understanding of hydrate morphology at the particle scale and its influence on stiffness evolution is required to confirm such viewpoint.

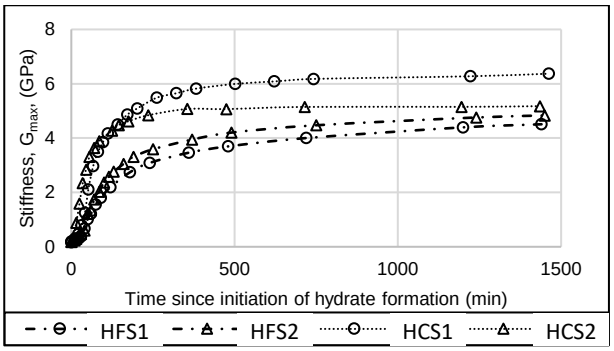

Figure 9. Stiffness evolution for HCS and HFS for different formation methods indicating much faster rate of stiffness development for the coarser sand. The time axis shown in minutes is for a better understanding of initial rate of evolution.

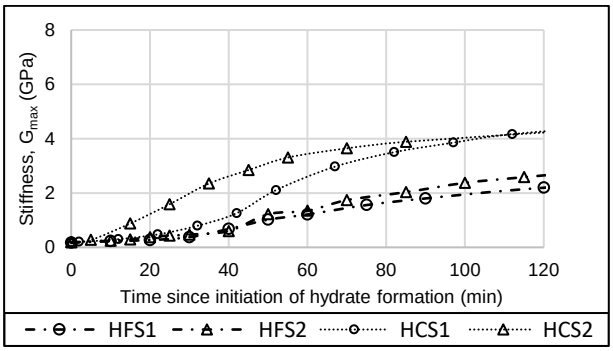

Figure 10. Initial increase in stiffness for HCS and HFS for different formation methods suggesting that the type of formation method chosen can affect the rate of stiffness evolution, and the behavior of coarser sands.

The initial stiffness evolution can also be used in understanding the role of different formation methods on the geomechanical behavior of HBS. As shown in Figure 10, the rate of stiffness evolution, which is related to the rate of hydrate formation, can be different for different sand mixtures depending on the type of formation. The stiffness evolution for pressure-driven (HFS2 and HCS2) is more rapid than for the temperature-driven (HFS1 and HCS1) likely due to the whole specimen being at the stability temperature (2°C) during pressure driven method compared to the difference caused by the propagation of cooling front from circumference to the inside for temperature driven. HCS seems to be more influenced by formation method chosen which could be due to more nucleation points as a result of water being at the contacts for HCS, thus the faster rate of stiffness evolution for pressure driven where the entire specimen is at same stability temperature. Therefore, the location and distribution of water as a result of different PSDs, and the difference in hydrate formation method are important parameters controlling the overall geomechanical behaviour of HBS.

The damping ratios measured during the hydrate formation process (Figure 11) also give important insights into the rate of hydrate formation and the morphology. The damping for HCS reduced more rapidly than for HFS specimen indicating a faster rate of water consumption (i.e., hydrate formation) for HCS specimen. The value of damping for HFS was initially higher than for HCS that might relate to more contacts experiencing squirt flow, suggesting patchy water distribution around the finer grains. This notable difference in damping behaviour during hydrate formation for different PSDs suggest that the hydrates in FS form relatively slow (Figure 9) and probably exist around the grains whereas for CS, most of the formation likely occurs at the grain contacts, leading to more nucleation points and thus the rapid damping due to rapid water consumption.

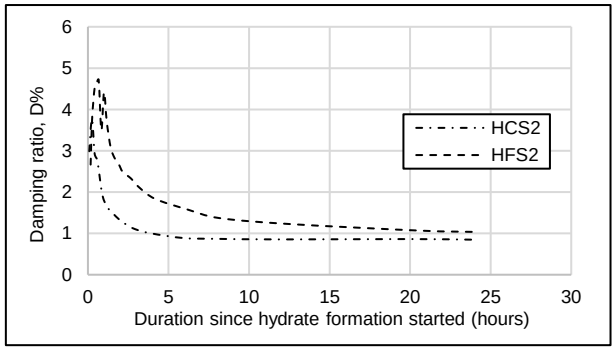

Figure 11. Comparison of damping for HCS and HFS for pressure driven formation method where the rate of damping reduces more rapidly for HCS indicating faster rate of hydrate formation.

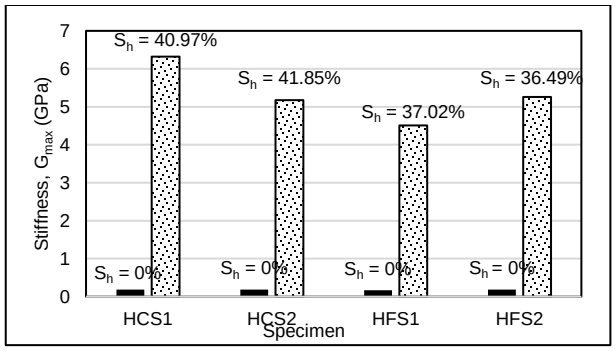

Figure 12. Final stiffness of all HBS indicating different level of influence on the behavior of HCS vs HFS with the introduction of hydrates in the pore space.

Figure 12 compares G_{max} for all 4 specimens before hydrate formation and their subsequent G_{max} after hydrate formation. For all the specimens the initial stiffness before hydrate formation is similar but after forming hydrates in the pore space, notable differences in final stiffness values for similar hydrate saturations are observed. The reason for these differences could be the stochastic nature of hydrate formation within a sand. More detailed studies are required to understand the significant differences in G_{max} for the same sands with similar hydrate saturations, as this suggests heterogeneity in hydrate distribution at the particle contact scale.

At the end of the hydrate formation stage, resonant column tests were also conducted under increasing cyclic strain (increased voltage to the drive head) to evaluate

shear modulus reduction behavior of the HBS. Figure 13 compares the shear modulus reduction (ratio of shear modulus (G) with G_{max}) for sand specimens with hydrates (HFS) and without hydrate (FS). As previously observed (Liu et al., 2021; Pandey et al., 2021), the formation of hydrate in the pore space leads to a reduction in the elastic threshold strain (the cyclic strain at which shear modulus reduces from G_{max}). There is also a corresponding increase in the damping ratio with increasing strain. Although hydrate increases the overall stiffness of the specimen, the reduced elastic threshold and increased damping might suggest the visco-elastic nature of hydrates.

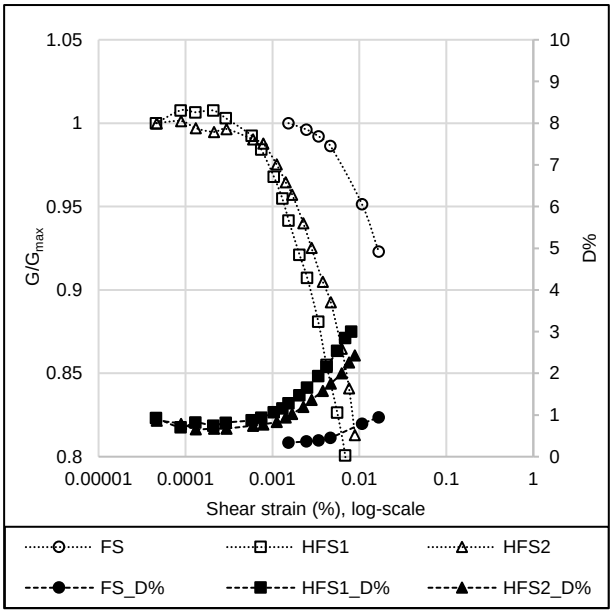

Figure 13. Modulus reduction curve and damping ratios for FS and HFS indicating lower elastic threshold for HBS, and show their dependency on the type of formation method.

4 CONCLUSIONS

This paper presents preliminary results from a study investigating the impact of hydrate formation method on the geomechanical behavior, of HBS with different particle size distributions. The tests on the two sands, without hydrate, highlighted minor variations in small-strain stiffness with particle size. Formation of methane gas-hydrate significantly increased the stiffness of each sand and show variations in the behavior between the two sands. It was observed that for CS specimens, the differences in stiffness for the two formation methods was 18%. For the FS specimens a smaller variation of 14% was observed.

Differences in the grain size distribution of the sands and the formation methods seem to have an affect on the formation rate and the final stiffness of HBS. This may relate to water distribution prior to hydrate formation, with FS sands that may have higher suctions leading to more patches of saturated sand grains and therefore less water concentrated at individual contacts. The differences in the small-strain stiffness also suggest the need to study and understand associated variations in large strain behavior that may result from how load is transferred through development of force chains, which in turn is the function of interaction between sand and hydrates. Understanding the differences in both small- and large-strain behavior for different sand mixtures as a result of different hydrate formation methods is important to more accurately evaluate the relationship between hydrate morphology and its influence on the heterogenic geomechanical response of natural HBS. It is anticipated that further tests will help consider these relationships in more detail.

5. ACKNOWLEDGEMENT

We would like to thank University of Calgary's Eyes High Doctoral Recruitment Scholarship, Natural Sciences and Engineering Research Council of Canada (NSERC) and Canadian Research Chairs Program for their financial support.

6. REFERENCES

Abbas, M. 2018. "Geomechanical characteristics of hydrate-bearing sands." MSc Thesis, University of Calgary, Canada.

ASTM D4015-15^{e1}. 2017. "Standard test methods for modulus and damping of soils by fixed-base resonant column devices."

Boswell, R. 2009. Is Gas Hydrate Energy Within reach? *Science*, 325(5943):957-958

Boswell, R. and Collett, T.S. 2011. Current perspectives on gas hydrate resources. *Energy Environ. Sci.* 4(4):1206-1215.

Boswell, R., Frye, M., Shelander, D., Shedd, W., McConnell, D.R., and Cook, A. 2012. Architecture of gas-hydrate-bearing sands from Walker Ridge 313, Green Canyon 955, and Alaminos Canyon 21: Northern deepwater Gulf of Mexico. *Mar. Pet. Geol.* 34: 134-149.

Boswell, R., Shipp, C., Reichel, T., Shelander, D., Saeki, T., Frye, M., Shedd, W., Collett, T.S. and McConnell, D. 2016. Prospecting for marine gas hydrate resources. Interpretation. *4. SA13-SA24. 10.1190/INT-2015-0036.1.*

Collett, T. S., Lee, M. W., Agena, W. F., Miller, J. J., Lewis, K. A., Zyrianova, M. V., Boswell, R., and Inks, T. L. 2011. Permafrost-associated natural gas hydrate occurrences on the Alaska North Slope. *Mar. Petrol. Geol*., 28(2), 279–294

Dai, S., Santamarina, J.C., Waite, W.F., and Kneafsey, T.J. 2012. Hydrate morphology: Physical properties of sands with patchy hydrate saturation. *J. Geophys. Res. Solid Earth*, 117**:** B11

Dallimore, S.R. and Collett, T.S. 2005. Scientific results from the Mallik 2002 Gas Hydrate Production Research Well Program, Mackenzie delta, Northwest Territories, Canada eds. *Geol. Sur. Can. B.* 585:957p.

Dallimore, S.R., Yamamoto, K., Waite, J.F., and Bellefleur, G. 2012. Proof of concept for gas hydrate production using the depressurization technique as established by the JOGMEC/NRCan/Aurora Mallik 2007-2008 gas hydrate production research well program. *Sci. res., eds. S.R. Dallimore, K. Yamamoto, J.F. Waite and G. Bellefleur, Geol. Sur. Can. B*. 601.

Dixit, G., Ram, H., and Kumar, P. 2019. Origin of gas in gas hydrates as interpreted from geochemistry data obtained during the National Gas Hydrate Program Expedition 02, Krishna Godavari Basin, offshore India. *Mar. Pet. Geol.* 108: 389-396.

Drnevich, V.P. 1978. Resonant Column Test. *Misc. Paper S-78-6, U.S. Army, D.C., U.S.A.* July 1978.

Flemings, P.B., Philips, S.C., Boswell, R. et al. 2020. Pressure coring of Gulf of Mexico deep-water turbidite gas hydrate reservoir: Initial results from The University of Texas – Gulf of Mexico 2-1 (UT-GOM2-1) hydrate pressure coring expedition. *AAPG Bulletin,* 104(9): 1847-1876.

Howard, J.J., Hester, K.C., Stevens, J.C. and Rydzy, M.B. 2011. Ultrasonic velocity measurements during experimental CH_4 hydrate formation and CO_2 exchange. *Proc. Seventh International Conference on Gas Hydrates*, Edinburgh, UK.

Hyodo, M., Yoneda, J., Li, Y., Nakata, Y., Yoshimoto, N., Nishimura, A. and Song, Y. 2013. Mechanical behaviour of gas-saturated methane hydrate-bearing sediments. *J. Geophys. Res. Solid Earth* 118(10):5185-5194.

Kida, M., Jin, Y., Watanabe, M. et al. 2015. Chemical and crystallographic characterizations of natural gas hydrates recovered from a production test site in the eastern Nankai Trough. *Mar. Pet. Geol.* 66: 396-403.

Kneafsey, T.J., Tomutsa, L., Moridis, G.J., Seol, Y., Freifeld, B.M., Taylor, C.E. and Gupta, A. 2007. Methane hydrate formation and dissociation in a partially saturated core-scale sand sample. *J. Pet. Sci. Eng.*, 56(1-3): 108-126.

Kumar, P., Collett, T., Yadav, U., Boswell, R., Cochran, J., Lall, M., Mazumdar, A., Ramana, M., Ramprasad, T., Riedel, M., Sain, K., Sathe, A., and Vishwanath, K. 2014. Geologic implications of gas hydrates in the offshore of India: Krishna-Godavari Basin, Mahanadi Basin, Andaman sea, and Kerala-Konkan basin. *J. Mar. Pet. Geol.* 58: 29-98.

Kurihara, M., Ouchi, H., Inoue, T., Yonezawa, T., Masuda, Y., Dallimmore, S.R., and Collett, T.S. 2005. Analysis of the JAPEX/JNOC/GSC et al. Mallik 5L-38 gas hydrate thermal-production test through numerical simulation. *In Scientific results from the Mallik 2002 gas hydrate production research well program, Mackenzie Delta, Northwest Territories, Canada, Geol. Sur. Can.*

Lei, L., Park, T., Jarvis, K. *et al.* 2022. Pore-scale observations of natiral hydrate-bearing sediments via pressure core sub-coring and micro-CT scanning. *Sci. rep.* 12: 3471.

Liu, Z., Kim, J., Hu, G., Hu, W., and Ning, F. 2021. Geomechanical property evolution of HBS under dynamic loads: Nonlinear behaviors of modulus and damping ratio. *Eng. Geol.* 295: 106427

Masui, A., Haneda, H., Ogata, Y. and Aoki, K. 2005. Effects of methane hydrate formation on shear strength of synthetic methane hydrate sediments. *In Fifteenth International Offshore and Polar Engineering Conference*, International Soc. Of Offshore and Polar Engineers:19-24.

Milkov, A.V. 2004. Global estimates of hydrate-bound gas in marine sediments: how much is really out there? *Earth Sci. Rev*. 66(3-4):183-197.

Minagawa, H., Ohmura, R., Kamata, Y., Nagao, J., Ebinuma, T., Narita, H. and Masuda, Y. 2009. Water permeability of porous media containing methane hydrate as controlled by the methane-hydrate growth process. *In T. Collett, A. Johnson, C. Knapp and R. Boswell eds., Natural gas hydrates – Energy resource potential and associated geologic hazards*, AAPG Memoir 89: 734-739.

Moore, M.T., Phillips, S., Cook, A.E., and Darrah, T.H. 2022. Integrated geochemical approach to determine the source of methane in gas hydrate from Green Canyon Block 955 in the Gulf of Mexico. *AAPG Bulletin.* 106(5): 949-980.

Moridis, G., Collett, T.S., Pooladi-Darvish, M., Hancock, S.H., Santamarina, C., Boswell, R., Kneafsey, T.J., Rutqvist, J., Kowalsky, M.B., Reagan, M.T., Sloan, E.D., Sum, A. and Koh, C. 2011. Challenges, uncertainties, and issues facing gas production from gas-hydrate deposits. *SPE Reserv. Eval. Eng.* 14(1):76-112.

Moridis, G.J., Reagan, M.T., Boswell, R., Collett, T.S. and Zhang, K. 2010. Preliminary evaluation of the production potential of recently discovered hydrate deposits in the Gulf of Mexico. *In Proc. of Offshore Technology Conference*, May 03-06, Texas, USA.

Moridis, G.J., Collett, T.S., Dallimore, S.R., Inoue, T. and Mroz, T. 2005. Analysis and interpretation of the thermal test of gas hydrate dissociation in the JAPEX/JNOC/GSC et al. Mallik 5L-38 gas hydrate production research well. *In Scientific Results, eds. S.R. Dallimore and T.S. Collett, Geol. Survey Can. B*. 585.

Myshakin, E.M., Seol, Y., Lin, J-S., Uchida, S., Collett, T.S., and Boswell, R. 2019. Numerical simulations of depressurization-induced gas production from an interbedded turbidite gas hydrate-bearing sedimentary section in the offshore India: Site NGHP-02-16 (Area-B). *Mar. Pet. Geol.* 108: 619-638.

Ouchi, H., Yamamoto, K., Akamine, K., Kano, S., Naili, M., Tamaki, M., Ohtsuki, S., Kanno, T., and Tenma, N. 2022. Numerical history-matching of modeling and actual gas production behavior and causes of the discrepancy of the Nankai Trough gas-hydrate production test cases. *Ener. Fuels.* 36: 210-226.

Pandey, M.R., Priest, J.A., and Hayley, J.L. 2021. Impact of particle size on the behavior of hydrate-bearing coarse-grained sands. *In Proc. 74th Canadian Geotech. Conf.,* Sept 26-29, Niagara, ON, Canada, 9 pages.

Priest, J. A., Rees, E.V.L. and Clayton, C.R.I. 2009. Influence of gas hydrate morphology on the seismic velocities of sands. *J. Geophys. Res. Solid Earth*, 114**:** B11205.

Priest, J.A., Best, A.I. and Clayton, C.R.I. 2005. A laboratory investigation into the seismic velocity of methane gas hydrate-bearing sand. *J. Geophys. Res. Solid Earth* 110(B4): B04102.

Priest, J. A., Rees, E.V.L. and Clayton, C.R.I. 2006. Attenuation of seismic waves in methane gas hydrate-bearing sand. *Geophys. J. Int.* 164: 149-159.

Priest, J.A., Hayley, J.L., Smith, W.E., Schultheiss, P. and Roberts, J. 2018. PCATS triaxial testing: Geomechanical properties of sediments from pressure cores recovered from the Bay of Bengal during expedition NGHP-02. *Mar. Pet. Geol.* 108: 424-438.

Priest, J.A., and Hayley, J.L. 2019. Strength of laboratory synthesized hydrate-bearing sands and their relationships to natural hydrate-bearing sediments. *J. Geophys. Res. Solid Earth*, 124(12): 12556-12575.

Sloan, E.D. and Koh, C.A. 2007. *Clathrate hydrates of natural gases*. 3rd Ed. CRC Press, T&F Group, NY, USA.

Spangenberg, E., Priegnitz, M., Heeschen, K. and Schicks, J.M. 2015. Are laboratory-formed hydrate-bearing systems analogous to those in nature? *J. Chem Eng. Data,* 60(2), 258-268.

Sultaniya, A., Priest, J.A. and Clayton, C.R.I. 2017. The impact of formation and dissociation conditions on the stiffness of hydrate-bearing sand. *Can. Geotech. J.* 55: 988-998.

Torres, M.E., Trehu, A.M., Cespedes, N., et al. 2008. Methane hydrate formation in turbidite sediments of northern Cascadia, IODP Expedition 311. *Earth Planet. Sci. Letters,* 271: 170-180.

Wallmann, K.E., Pinero, E., Burwicz, E., Haeckel, M., Hensen, C., Dale, A., and Ruepke, L. 2012. The global inventory of methane hydrate in marine sediments: A theoretical approach. *Energies,* 5: 2449-2498.

Yamamoto, K., Terao, Y., Fujii, T., Ikawa, T., Seki, M., Matsuzawa, M. and Kanno. T. 2014. Operational overview of the first offshore production test of methane hydrates in the Eastern Nankai Trough. *In Proc. of Offshore Technology Conference*, May 05-08, Houston, Texas.

Yang, S., Liang, J., Lei, Y., Gong, Y., Xu, H., Wang, H., Lu, J., Holland, M., Schultheiss, P., and Wei, J. 2017. GMGS4 gas hydrate drilling expedition in the South China Sea. *Fire Ice.* 17(1): 7-11.

Yoneda, J., Kida, M., Konno, Y., Jin, Y., Morita, S., and Tenma, N. 2019. In situ mechanical properties of shallow gas hydrate deposits in the deep seabed. *Geophys. Res. Letter*, 46: 14,459-14,468.

Yun, T.S., Santamarina, J.C. and Ruppel, C. 2007. Mechanical properties of sand, silt, and clay containing tetrahydrofuran hydrate. *J. Geophys. Res. Solid Earth*, 112(B04106):1-13.